Chemical Science

EDGE ARTICLE

View Article Online
View Journal | View Issue

Check for updates

Cite this: *Chem. Sci.*, 2025, **16**, 19792

All publication charges for this article have been paid for by the Royal Society of Chemistry

Tailoring the electronic structure to enable rapid Li-ion diffusion and a stabilized LiF–LiCl rich electrode–electrolyte interface

Shan Su,[a] Xuanyi Zhou,[a] Weizhong Liang,[a] Zhuoriu Su,[a] Yibing Qu,[a] Yuhan Zhong,[a] Jinghong Qiu[a] and Biao Zhang *[ab]

Received 15th July 2025
Accepted 18th September 2025

DOI: 10.1039/d5sc05254h

rsc.li/chemical-science

The chemical composition of the solid electrolyte interphase (SEI) at the Li anode/electrolyte interface is critical to the performance of lithium metal batteries. Herein, we designed a functional ionic salt (DG-Cl) with a π-conjugated structure, aiming to enhance the electronic delocalization of the filler to regulate the bond-breaking kinetics and promote the formation of the effective components of the SEI. Density functional theory (DFT) verifies that DG-Cl is capable of releasing Cl^- directionally under an electric field and subsequently combining with Li^+ to form LiCl. Simultaneously, DG-Cl can anchor $TFSI^-$ *via* cation vacancies. Besides, through its strong electron delocalization capability, DG-Cl could facilitate the cleavage of C–F bonds of $TFSI^-$ during the binding process (with charge transfer reaching up to $1.8453e^-$), thereby promoting the formation of more LiF. XPS and TOF-SIMS confirmed the *in situ* uniform co-growth of LiF–LiCl on the SEI, which facilitates the Li-ion transport kinetics and regulates the lithium deposition behavior. Impressively, the lithium symmetric batteries deliver ultralong cycling stability over 4000 hours at 0.1 mA cm^{-2} and over 2200 hours at 0.2 mA cm^{-2} while the Li/$LiFePO_4$ full cells possess 82.04% capacity retention after 800 cycles at 2C. Besides, this approach to regulating electron transfer at the molecular level guarantees the outstanding cycling performance of pouch cells. After 150 cycles, the battery retention rate was 96.6%. This work proposes a new approach to achieving high-performance and stable lithium metal batteries (LMBs).

1 Introduction

All-solid-state lithium-metal batteries (ASSLMBs) are a top candidate for future energy storage and they offer two key benefits: inherent safety and superior energy density.[1,2] Polymer solid electrolytes have garnered significant research interest due to their outstanding flexibility and processability.[3,4] However, the lithium anode's high reactivity leads to continuous electrolyte side reactions. This results in an unstable SEI layer that repeatedly breaks down and reforms.[5,6] This continuous process consumes both the electrolyte and lithium ions, thereby increasing resistance and causing a decline in battery capacity.[7] In addition, the fragile SEI lacks the mechanical strength and electronic insulation necessary to suppress electron tunneling and regulate ion flux. As a result, uneven lithium deposition and rampant dendrite growth result in deteriorated cycle life.[8] Consequently, the rational design and construction of a stable SEI layer is crucial for improving overall battery performance.[9–11]

LiF is widely regarded as an optimal SEI component due to its sufficiently low Li^+ diffusion barrier and exceptional mechanical strength.[12] Typically, LiF arises from the cleavage of the C–F bond within the anion of lithium salts present in the electrolyte.[13] Therefore, precisely controlling the kinetics of C–F bond cleavage is essential for constructing a LiF-rich SEI layer. This can be achieved through various strategies, such as introducing polar functional groups to enhance charge transfer efficiency or creating charge storage reservoirs to enhance the charge transfer numbers, both of which promote the formation of a robust LiF-rich SEI layer. Li and his team introduced polar functional groups (C═O), thereby inducing electron transfer to LiTFSI and promoting C–F bond breakage, ultimately leading to LiF formation.[14] Chen *et al.* constructed a LiF-rich SEI by introducing porphyrin-based covalent organic frameworks (COFs), which induced the cleavage of $TFSI^-$ through electronic redistribution within the hetero-segments of the structural nodes.[15] However, due to F^- strong electronegativity, LiF exhibits low Li^+ conductivity ($\approx 10^{-31}$ S cm^{-1}), which significantly hinders lithium ion transport at the electrode interface, thereby increasing the interfacial impedance of the battery.[16] This can result in significant polarization effects during

---

[a] *Key Laboratory of Low Dimensional Materials and Application Technology of Ministry of Education, School of Materials Science and Engineering, Xiangtan University, Hunan 411105, China. E-mail: biaozhang@xtu.edu.cn*

[b] *Hunan Provincial Key Laboratory of Thin Film Materials and Devices, School of Materials Science and Engineering, Xiangtan University, Xiangtan 411105, China*

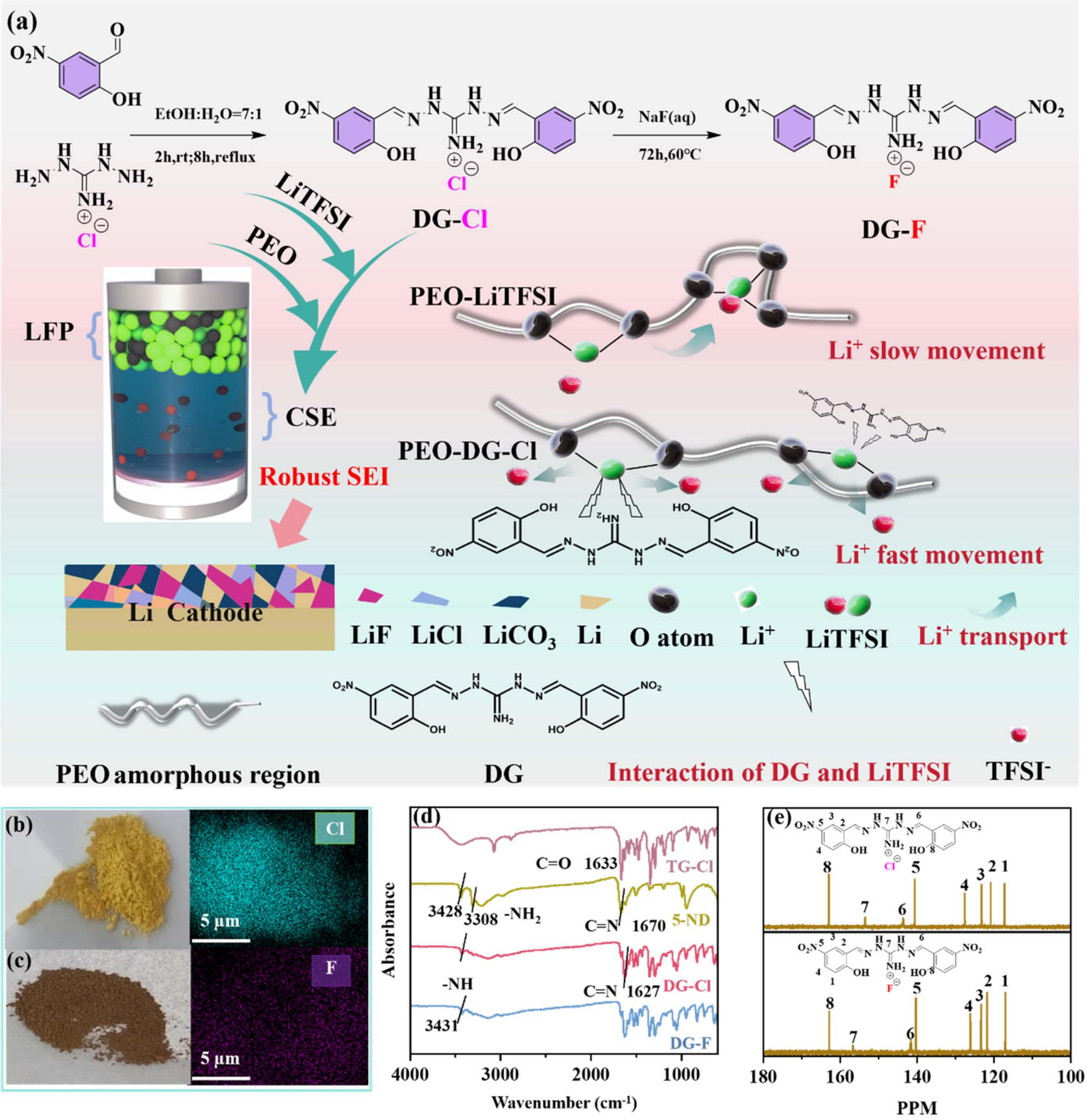

Fig. 1 (a) Schematic illustrating filler preparation procedures and its mechanism of action in electrolytes. SEM and EDS of the powders. (b) DG-Cl. (c) DG-F. (d) The FTIR of the reactive monomers TG-Cl and 5-ND, as well as the synthesized compounds DG-Cl and DG-F. (e) ^{13}C NMR of powders DG-Cl and DG-F.

charging and discharging, which may lead to premature battery failure.[17,18] By designing fillers with electronic delocalization capabilities, it is possible to catalyze the formation of other inorganic components with high Li^+ conductivity at the molecular level. This approach can effectively address the drawbacks brought about by a single LiF-rich SEI and simultaneously enhance the interface stability of the battery.

In recent years, LiCl has attracted considerable attention as a vital component of the electronically insulating SEI, owing to its outstanding ionic conductivity ($\approx 10^{-8}$ S cm^{-1}),[19] wide electrochemical stability window, and effective barrier against lithium-ion migration.[20] Wu *et al.* developed a mechanically flexible yet rigid bi-protective layer composed of a LiCl-rich SEI on a lithium anode. This layer not only mitigates dendrite growth but also promotes rapid Li^+ transport, leading to uniform lithium deposition.[21] However, the SEI layer predominantly consisting of LiCl exhibits poor mechanical strength with a Young's modulus of approximately 50 GPa and struggles to accommodate volume changes during repeated lithium plating/stripping cycles.[22,23] This inherent brittleness renders it susceptible to cracking and exposes fresh lithium surfaces, consequently triggering dendrite growth.[24,25] As an essential component of the SEI, LiF exhibits strong mechanical strength, which can effectively compensate for the shortcomings of LiCl. Therefore, the combination of LiCl and LiF can significantly enhance interface stability and further enhance the electrochemical performance of the battery.

In this study, we developed a weakly bonded cationic organic ionic salt (DG-Cl), as depicted in Fig. 1a. Subsequently, the synthesized ionic salts (DG-Cl and DG-F) were incorporated as functional fillers into the PEO-LiTFSI matrix to fabricate a composite electrolyte material. This composite SEI layer synergistically leverages the excellent mechanical stability of LiF and the high ionic conductivity of LiCl, thereby concurrently enhancing the mechanical robustness, electrochemical stability, and lithium-ion transport kinetics of the interfacial film. The *in situ* growth of the LiF–LiCl SEI at the Li/electrolyte interface was confirmed by XPS/TOF-SIMS analysis. First-principles calculations combined with AIMD simulations have revealed the *in situ* growth mechanisms of LiF and LiCl through the DG-Cl dual functional roles of electron transfer and electron anchoring. DG-Cl can reduce Li^+-$TFSI^-$ complexation strength, enhancing lithium-ion liberation and enabling efficient C–F bond dissociation *via* electron transfer mechanisms. Simultaneously, under the influence of an electric field, Cl^- undergoes ionization and subsequently combines with free Li^+ to form LiCl, leading to the formation of a LiF–LiCl hybrid SEI layer at the Li/SPE interface, which facilitates the Li-ion transport kinetics and regulates the lithium deposition behavior. Compared with Li symmetric cells with the single LiF-rich SEI, those with the LiF–LiCl rich SEI demonstrated prolonged cycling stability exceeding 4000 hours at 0.1 mA cm^{-2}, significantly outperforming the single LiF-rich SEI, which failed after approximately 2200 hours. Additionally, the PEO-DG-Cl full cell retains a capacity of 82.04% after 800 cycles at 1C and 80.6% after 800 cycles at 2C. Moreover, it shows good cycling performance at room temperature.

2 Results and discussion

2.1 Structural characterisation of DG-Cl and DG-F

The synthesis of the target compound DG-Cl is predicated on the Schiff base reaction between 5-nitrosalicylaldehyde (5-ND) and diaminoguanidine hydrochloride (TG-Cl),[26] as illustrated in Fig. 1a. To validate the synthesis process and elucidate the structure of the resultant product, we conducted comprehensive characterization utilizing Fourier transform infrared spectroscopy (FTIR) and nuclear magnetic resonance spectroscopy (NMR). The FTIR spectrum shown in Fig. 1d indicates that the characteristic peak of the $-C{=}O^-$ group from the 5-ND monomer at 1662 cm^{-1}, as well as the peaks corresponding to the primary amine group ($-NH_2^-$) of TG-Cl at 3428 and 3308 cm^{-1}, completely vanished after the reaction. A new bending vibration peak for $-NH^-$ appeared at 3431 cm^{-1}. This suggests that the $-NH_2^-$ and $-C{=}O^-$ groups underwent a chemical reaction leading to structural reconfiguration. Notably, the stretching vibration peak of the $-C{=}N^-$ bond shifted to 1627 cm^{-1}. This provides direct evidence that an imine bond ($-C{=}N^-$) was formed through the condensation of the aldehyde group of 5-ND and the amino group of TG-Cl.[27] Further structural analysis was conducted using ^{13}C NMR analysis (Fig. 1e). The results showed that the characteristic peaks located at positions 1–5 and position 8 corresponded to carbon signals from benzene rings present in the DG-Cl structure. The peak observed at 156.72 ppm was attributed to carbon atoms within guanidine groups.[28] Additionally, a newly identified peak at 141.71 ppm distinctly indicated the formation of $-C{=}N^-$ bonds resulting from reactions between aldehyde groups and amino groups.[29] Both spectroscopic techniques demonstrated remarkable consistency in their structural characterization, thereby conclusively affirming successful synthesis of DG-Cl alongside accuracy regarding its molecular architecture.

After the ion exchange reaction, ^{13}C NMR signals at positions 6 and 7 exhibit significant shifts. This phenomenon can be attributed to the strong electronegativity of F^-, which induces a reconfiguration of the local electronic environment. The carbon atom at position 7 experiences a shift to a lower field (higher chemical shift value), reflecting diminished electron density due to the electron-withdrawing nature of F^-.[30] Conversely, the carbon atom at position 6 shifts to a higher field, likely as a result of compensating electronic effects from adjacent groups.[31] Fig. 1b and c illustrate that following ion exchange, the color of the powder sample changes from yellow to brown. The EDS spectrum confirms that fluorine is uniformly distributed within the DG-F powder, while Fig. S1 demonstrates an absence of chlorine in the DG-F powder. This indicates that Cl^- has been completely replaced by F^-, thereby validating the reliability of the ion exchange process.

2.2 Physical and electrochemical testing of composite solid-state electrolytes (CSEs)

Li^+ migrates through segmental motion within the amorphous regions of polymers,[32] thus the crystallinity of polymer electrolytes critically governs their Li^+ transport capability. As shown in Fig. 2a, the crystallization behavior of CSEs was investigated using X-ray diffraction (XRD). The XRD pattern reveals that the PEO-LiTFSI system exhibits distinct diffraction signals at 19.2° and 22.2°, indicating a highly ordered crystalline structure within this system. In contrast, the characteristic peaks of PEO-DG-Cl, PEO-TG-Cl, and PEO-DG-F are significantly diminished or even absent, suggesting effective suppression of the crystallization behavior of the polymer matrix. Notably, the intensity decay of the diffraction peak for PEO-DG-Cl electrolyte is particularly pronounced. This may be ascribed to strong Lewis acid–base interactions formed between electron-rich groups (guanidinium) in DG fillers and PEO chain segments,[33] which disrupts the orderly stacking of polymer chains through coordination effects. Furthermore, Cl^- possesses a larger ionic radius compared to F^-, resulting in greater steric hindrance on PEO chain segments and thereby promoting an expansion of amorphous regions.[34–36] As shown in Fig. 2b, the crystallization

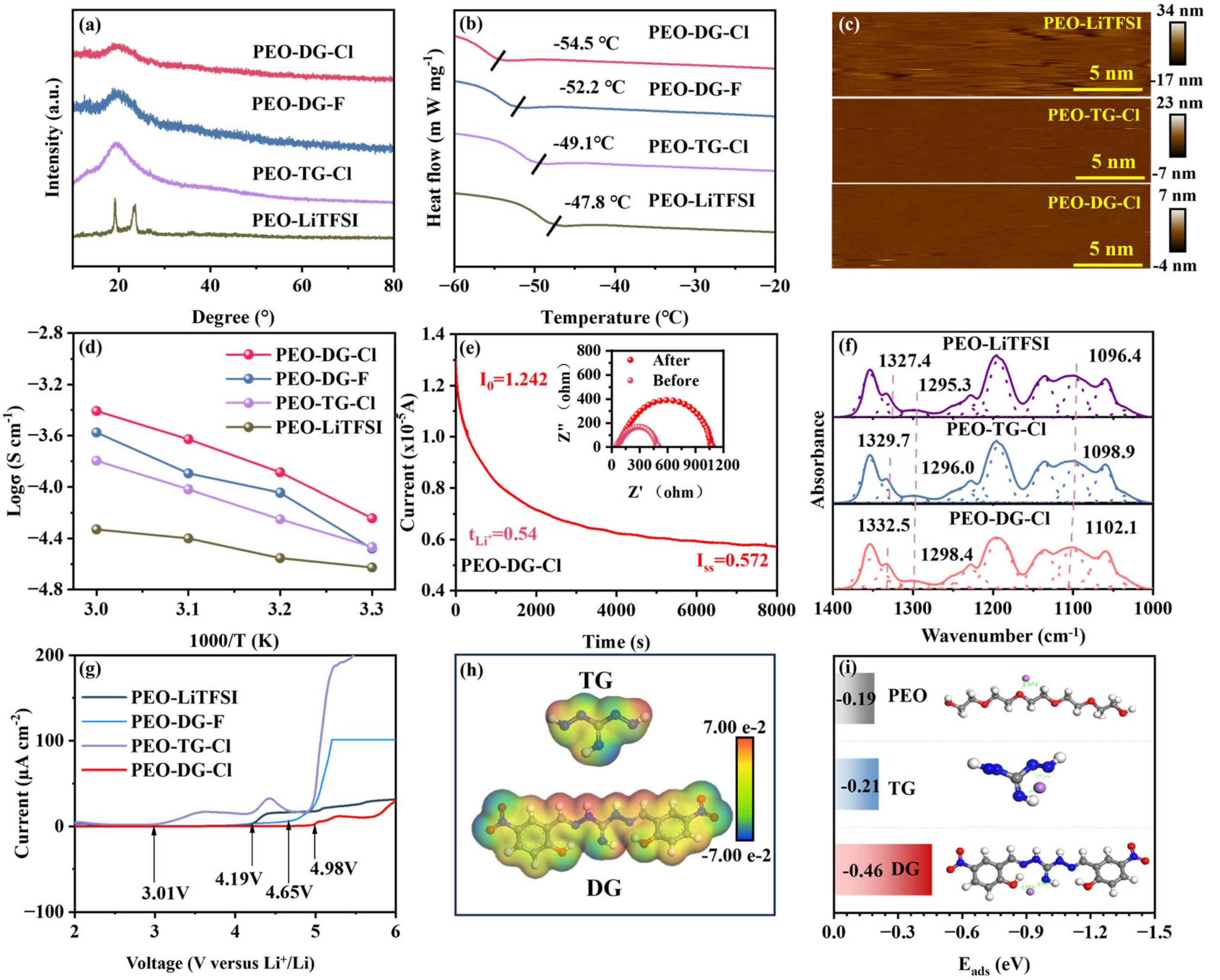

Fig. 2 (a) XRD spectra. (b) DSC curves. (c) AFM image of the CSE surface. (d) Ionic conductivity of CSEs. (e) Li$^+$ mobility number curves of PEO-DG-Cl. (f) CSE Fourier infrared curve. (g) LSV curve. (h) TG and DG electrostatic potential distributions. (i) Binding energies of PEO chains, TG, and DG with lithium ions.

behavior of CSEs was further analyzed using Differential Scanning Calorimetry (DSC). The DSC curves indicate that the glass transition temperatures (T_g) for PEO-DG-Cl, PEO-DG-F, and PEO-TG-Cl are −54.5 °C, −52.2 °C, and −49.1 °C, respectively, while the T_g value for pure PEO-LiTFSI is −47.8 °C. The observed decrease in T_g values indicates an increase in amorphous regions within the electrolyte and enhanced segmental mobility, which is consistent with the results from XRD, where a reduction in crystallization peaks was noted. Meanwhile, the reduction in crystallinity will have a substantial impact on its surface morphology. The microstructures of the CSEs were characterized using atomic force microscopy (AFM). As depicted in Fig. 2c, the unmodified PEO electrolyte displays significant roughness, characterized by numerous pits and wrinkles. In contrast, the surface roughness of the PEO-TG-Cl and PEO-DG-Cl electrolytes modified with TG-Cl and DG-Cl is markedly reduced, resulting in a smoother and denser surface morphology. This smooth and uniform electrolyte film promotes intimate interfacial adhesion with lithium metal cathodes.

Higher ionic conductivity and lithium-ion transport numbers can alleviate the polarization effects in batteries, thereby promoting the rapid migration of Li$^+$.[37] To enhance the ionic conductivity of the electrolyte and determine the ideal filler proportion, SS/CSEs/SS batteries were assembled to assess the ionic conductive properties of the CSEs. Fig. S2 illustrates the impedance characteristics of CSEs with varying filler contents at different temperatures (30, 40, 50, and 60 °C), measured by AC impedance spectroscopy. As temperature increases, the impedance of the electrolyte decreases correspondingly, leading to an increase in its ionic conductivity. Utilizing the Arrhenius equation, further fitting was performed on the impedance data to calculate ionic conductivity values. When the filler content was set at 1 wt%, a peak in ionic conductivity was observed, indicating that this level represents an optimal addition. Fig. 2d presents the temperaturedependent ionic conductivities of CSEs containing 1 wt% PEO-TG-Cl, PEO-DG-Cl, PEO-DG-F, and pure PEO-LiTFSI. Compared with PEO (2.36×10^{-5} S cm^{-1} at 30 °C), the ionic conductivities of PEO-DG-Cl, PEO-DG-F, and PEO-TG-Cl increased to 8.20×10^{-5} S cm^{-1}, 5.55×10^{-5} S cm^{-1}, and 3.41×10^{-5} S cm^{-1}, respectively. As the temperature increases to 60 °C, substantially improves chain segment mobility. The ionic conductivity of pure PEO only improves to 4.68×10^{-5} S cm^{-1}, while that of the PEO-DG-Cl electrolyte markedly rises to reach a value of up to 3.48×10^{-4} S cm^{-1}, substantially higher than that of conventional PEO electrolytes as well as those for PEO-DG-F (2.57×10^{-4} S cm^{-1}) and PEO-TG-Cl (1.6×10^{-4} S cm^{-1}).

The lithium-ion transfer number (t_{Li^+}) for assembled Li/CSEs/Li batteries was determined using the Bruce–Vincent method. As shown in Fig. 2e, the t_{Li^+} value for PEO-DG-Cl is 0.54, which is significantly higher than those of PEO-DG-F, PEO-TG-Cl, and PEO-LiTFSI, with t_{Li^+} values of 0.32, 0.30, and 0.15, respectively (Fig. S3). This phenomenon occurs because the DG-Cl cation has the ability to adsorb and anchor TFSI$^-$, which in turn facilitates the dissociation of lithium salts, leading to an increased release of Li$^+$.

To explore the influence of TG and DG fillers on the dissociation of LiTFSI, the FTIR spectra of pure PEO, PEO-TG-Cl, and PEO-DG-Cl within the wavelength range of 1400–1000 cm^{-1} were compared, as illustrated in Fig. 2f. The PEO-LiTFSI CSEs displayed characteristic $-SO_2^-$ symmetric and asymmetric stretching modes at 1327.4 cm^{-1} and 1295.3 cm^{-1}, respectively. Upon introducing fillers, the $-SO_2^-$ stretching vibration peaks for PEO-TG-Cl shifted to 1329.7 cm^{-1} and 1296.0 cm^{-1}, while those for PEO-DG-Cl moved to 1332.5 cm^{-1} and 1298.4 cm^{-1}. Notably, the $-CF_3^-$ vibration peak exhibited a significant shift from 1096.4 cm^{-1} in PEO-LiTFSI to 1098.9 cm^{-1} in PEO-TG-Cl, with a further displacement to 1102.1 cm^{-1} in PEO-DG-Cl. The changes observed in these two peaks are more evident in the PEO-DG-Cl electrolyte, indicating that DG interacts more strongly with TFSI$^-$. This interaction consequently facilitates the dissociation of LiTFSI and enhances Li$^+$ release.

The electrochemical window serves as a critical indicator for assessing electrolyte performance and practical usability.[38] Fig. 2g presents the linear sweep voltammetry (LSV) curves of four different solid polymer electrolytes that were prepared. The oxidation current of PEO-LiTFSI shows a significant increase at 4.19 V, leading to subsequent decomposition of the electrolyte. In contrast, PEO-DG-Cl exhibits superior oxidative stability, with an electrochemical window of approximately 4.98 V, surpassing that of PEO-DG-F (4.65 V). Notably, the electrochemical window of PEO-TG-Cl is only 3.01 V, which is even lower than that of pure PEO. This indicates that the incorporation of unmodified small molecules not only fails to protect the electrolyte from oxidation and decomposition but may also trigger strong side reactions with PEO, resulting in premature degradation.

To investigate the coordination mechanism of TG and DG molecules with lithium salts, we systematically calculated the molecular electrostatic potential distribution and binding energy based on DFT. The electrostatic potential mapping in Fig. 5e demonstrates that the long-chain segment of DG exhibits a stronger positive charge compared to TG. Notably, there is a significant increase in electrostatic potential energy around the guanidine chain segment at the center of the molecule. The binding energy calculations presented in Fig. 5f reveal that DG's binding energy with Li$^+$ reaches −0.46 eV, which significantly exceeds that of traditional PEO-based electrolytes (−0.19 eV) and TG molecules (−0.21 eV). This discovery suggests that the extension of the π-conjugated structure can substantially improve the charge binding capacity of DG. Furthermore, strong coordination between the central part of DG and TFSI$^-$ weakens the coulombic interaction between Li$^+$-TFSI$^-$ ion pairs, thereby remarkably promoting the dissociation of LiTFSI.

2.3 Testing the interfacial stability of lithium metal batteries

To investigate the effects of incorporating DG-Cl on the stability of interfaces, symmetric Li/Li batteries incorporating various solid electrolytes were cycled at 60 °C. The stability of the electrolyte film was assessed at 0.1 mA cm^{-2} current density, as illustrated in Fig. 3a. The PEO-LiTFSI symmetrical cell exhibited limited cycling stability with a 200 hour lifespan, and the cycle lifetimes of PEO-DG-F and PEO-DG-Cl symmetrical cells surpass 2400 hours and 4000 hours, respectively, without any occurrence of short-circuit phenomena. Even at elevated 0.2 mA cm^{-2} current density, the PEO-DG-Cl cell continues to exhibit stable cycling for over 2000 hours (Fig. 3c). By comparing the performance of various reported CSEs in Li/Li symmetric cells at 60 °C (Fig. 3b),[39–51] the exceptional interfacial stability exhibited by the PEO-DG-Cl system in this study was further substantiated. Furthermore, we analyzed the lithium deposition/stripping voltage profiles for both Li/PEO-DG-Cl/Li and Li/PEO-DG-F/Li symmetrical cells across varying current densities (0.1–0.5 mA cm^{-2}). As depicted in Fig. 3e, the Li/PEO-DG-Cl/Li cell maintains a low and stable polarization voltage throughout the entire deposition/stripping process, significantly lower than that of the PEO-LiTFSI and PEO-DG-F cells.

The critical current density signifies the maximum current density that a symmetrical lithium battery can endure.[52] The detailed voltage–time curves of three groups of Li/Li symmetrical batteries were evaluated at 60 °C. As the current density increased, the polarization voltage correspondingly rose. As illustrated in Fig. 3d and S4, the critical current density for the PEO-DG-Cl based symmetrical lithium battery reaches 1.23 mA cm^{-2}, whereas that for the PEO-DG-F based symmetrical lithium battery reaches 0.92 mA cm^{-2}. Notably, the simple PEO-LiTFSI system experiences short-circuiting at 0.5 mA cm^{-2}. A higher critical current density (CCD) signifies superior suppression of lithium dendrite growth because it represents the electrolyte's enhanced ability to maintain uniform Li-ion flux and deposition at high current densities, thereby delaying the onset of detrimental space charge effects and localized dendrite initiation that occur when the limiting current is exceeded, which confirms that the PEO-DG-Cl electrolyte can effectively inhibit lithium dendrite formation.

To assess the influence of DG-Cl on lithium deposition behavior, assembled Li/CSE/Cu cells were subjected to further

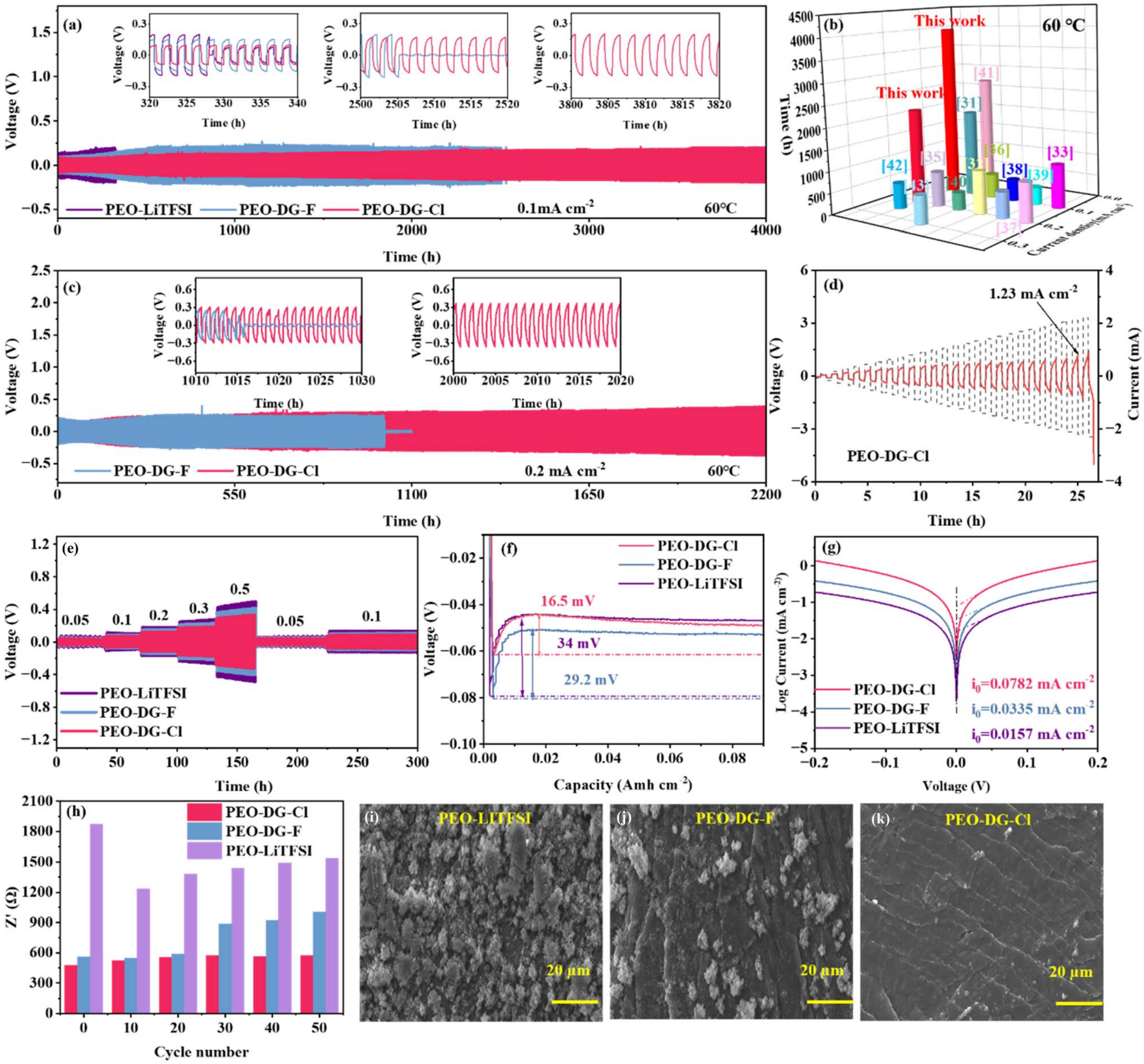

Fig. 3 (a) Galvanostatic cycling profiles for Li/Li symmetric cells operated at 0.1 mA cm^{-2} current density with 0.1 mAh cm^{-2} capacity. (b) Comparative analysis of long-term cycling performance of Li/Li symmetric full cells at 60 °C. (c) Charge–discharge characteristics of Li/Li symmetric cells at 0.2 mA cm^{-2} current density and 0.1 mAh cm^{-2} capacity. (d) CCD testing of PEO-DG-Cl symmetric cells. (e) Electrochemical cycling responses of Li/Li symmetric cells across varied current densities. (f) Lithium plating/stripping nucleation overpotentials for Li/Li symmetric cells. (g) Li/Li symmetric cell Tafel curves. (h) Electrochemical impedance spectroscopy data for Li/CSEs/Li batteries recorded pre-cycling and following 1–50 charge–discharge cycles. Surface morphology analysis *via* SEM for lithium electrodes in (i) PEO-LiTFSI. (j) PEO-DG-F. (k) PEO-DG-Cl electrolyte systems.

testing. As depicted in Fig. 3f, the nucleation overpotentials for PEO-LiTFSI, PEO-DG-F, and PEO-DG-Cl during the initial stages of lithium deposition are recorded at 29.2 mV, 24 mV, and 16.5 mV, respectively. It is noteworthy that among the CSEs studied, PEO-DG-Cl demonstrates the lowest nucleation overpotential. This finding suggests that the interfacial layer between PEO-DG-Cl and lithium metal exhibits minimal nucleation resistance during the lithium deposition and desorption processes, thereby significantly facilitating the migration of Li$^+$ at the interface. The exchange current density serves as a crucial parameter for investigating the kinetics of the lithium deposition reaction.[53] As illustrated in Fig. 3g, PEO-DG-Cl demonstrates an impressive exchange current density of 0.0782 mA cm^{-2}, superior performance compared to PEO-LiTFSI, which has a value of 0.0157 mA cm^{-2}, by 389%. Furthermore, it exceeds the performance of PEO-DG-F, recorded at 0.0225 mA cm^{-2}, by an outstanding margin of 247%. This elevated exchange current density suggests that the PEO-DG-Cl electrolyte facilitates charge transfer processes at the Li/CSE interface, thereby enhancing Li$^+$ transport kinetics.

To evaluate the evolution of interface impedance, symmetric Li/CSE/Li configurations underwent electrochemical impedance spectroscopy analysis across multiple cycles (0–50 cycles). The interfacial impedance exhibited dynamic changes over time at a constant current density. As illustrated in Fig. 3h and S5, the initial interfacial impedance between PEO-DG-Cl and metallic lithium is significantly lower at 477 Ω compared to that of Li/PEO-LiTFSI/Li, which measures 1872 Ω, and Li/PEO-DG-F/Li at 558 Ω. The interfacial impedance between PEO-DG-Cl and metallic lithium shows a slight increase over time, stabilizing at 562 Ω after 40 cycles. In contrast, the interfacial impedance for PEO-DG-F with metallic lithium remains unstable beyond the 40 hour mark, rising to 1005 Ω after 50 cycles. Meanwhile, the interfacial impedance for PEO-LiTFSI reached 1533 Ω after 50 cycles. The interfacial layer between the PEO-DG-Cl electrolyte and the lithium anode significantly enhances interface stability, facilitates the migration of lithium ions, and consequently reduces overall interfacial impedance. To demonstrate the influence of DG-Cl on the regulation of lithium metal electrodeposition behavior, 200 hour cycling tests were performed on symmetrical lithium batteries utilizing various CSEs. The morphology of lithium deposition was examined using scanning electron microscopy (SEM), as shown in Fig. 3i–k. The samples combined with PEO electrolytes exhibit lithium anodes with porous, dendritic architectures featuring vertically oriented growth patterns and flaky inactive lithium accumulation. In contrast, within PEO-DG-F, while there was a noticeable reduction in spherical dendrites leading to an uneven surface on the lithium metal, some cracks remained present. Remarkably, PEO-DG-Cl enabled homogeneous lithium deposition, yielding smooth electrode surfaces devoid of dendrites or dead lithium.

2.4 Analysis of SEI characterization and formation mechanisms

Generally speaking, the stability and performance of battery interfaces are significantly influenced by the composition and structure of the SEI. Based on this understanding, lithium metal strips were extracted from Li/PEO-LiTFSI/Li, Li/PEO-TG-Cl/Li, Li/PEO-DG-Cl/Li, and Li/PEO-DG-F/Li batteries after 200 hours of cycling. X-ray photoelectron spectroscopy (XPS) was employed to investigate the SEI components present on these disassembled lithium strips. As shown in Fig. 4a, the C 1s spectrum reveals decomposition peaks at 284.7 eV (C–C/C–H) and 286.5 eV (C–O),[54,55] These peaks primarily arise from the decomposition of PEO. It is evident that introducing fillers into CSEs effectively mitigates PEO decomposition. Fig. 4b displays characteristic peaks located at 684.8 eV (LiF) and 688.7 eV (C–F moieties including CF_2/CF_3).[56,57] In comparison, the characteristic peaks for LiF and CF_2 in the lithium strip from the Li/PEO-DG-Cl/Li and Li/PEO-DG-F/Li batteries are notably higher. This indicates that incorporating DG facilitates cleavage of TFSI-bound C–F bonds, thereby increasing the abundance of CF_2 radicals which leads to enhanced formation of more LiF. Additionally, Cl 2p spectra reveal characteristic binding energies at 197.8 eV and 199.6 eV (Fig. 4c),[58] which correspond to LiCl formation within SEIs generated in Li/PEO-DG-Cl/Li and Li/PEO-TG-Cl/Li batteries.

To further investigate spatial distribution characteristics between LiF and LiCl within SEIs formed during operation, three-dimensional compositional mapping of lithium metal anode surfaces was performed *via* time-of-flight secondary ion mass spectrometry (TOF-SIMS) analysis, as depicted in Fig. 4d. Notably, for the Li/PEO-DG-F/Li battery configuration, it is important to mention that LiTFSI is not the sole source of fluorine. The highest concentration of LiF was observed in the PEO-DG-F electrolyte, resulting in the formation of the thickest SEI layer. However, an excessively thick SEI layer can lead to increased lithium-ion diffusion impedance, which may adversely affect both the lifespan and safety of the battery.[59] The SEI formed in the Li/PEO-DG-Cl/Li battery exhibits a moderate thickness, with relatively high concentrations of LiF and LiCl that are more uniformly distributed. Fig. 4e–f illustrate cross-sectional images exhibiting high lateral resolution across interfaces containing LiF_2^- and $LiCl_2^-$, suggesting that introduction of DG-Cl catalyzes dissociation processes involving LiTFSI and the shedding of Cl^-, thus enabling co-growth phenomena between LiF–LiCl layers constituting SEIs.

To elucidate the formation mechanism of a robust LiF–LiCl SEI layer, SS/CSEs/Li cells were assembled initially and cyclic voltammetry (CV) tests were prepared to examine the influence of DG on the catalytic decomposition of LiTFSI. Electrochemical characterization performed *via* CV highlights distinct redox behaviors in the three batteries, as depicted in Fig. 5a–c. Each specimen demonstrates a characteristic reduction signal between 1.2 and 1.5 V, which corresponds to the decomposition peak of $TFSI^-$. The intensity of this $TFSI^-$ reduction peak is directly proportional to the extent of its catalytic decomposition. By analyzing the CV cycling curves obtained from various electrolytes, it is observed that in the PEO-TG-Cl electrolyte, the decomposition peak for $TFSI^-$ remains evident throughout all cycles. In contrast, in the PEO-DG-Cl electrolyte, there is a pronounced intensity in $TFSI^-$ reduction, indicating that DG-Cl effectively catalyzes the decomposition process of $TFSI^-$, leading to an increased generation of F^- and consequently more LiF production. To achieve a more profound understanding of the catalytic mechanism of DG-Cl, the Bader charges of TG and DG were calculated using the charge density difference method and the charge transfer process of DG on LiTFSI was examined. As illustrated in Fig. 5g, when $TFSI^-$ interacts with DG-Cl and TG, it pairs with the Lewis site on the cation, resulting in a transfer of charge to $TFSI^-$. Notably, the charge transfer number for TG-Cl is only $0.10584e^-$. In contrast, the structure-optimized DG-Cl exhibits a charge transfer number of $1.8452e^-$, which is 17 times greater than that of TG-Cl. This significant disparity can be attributed to intermolecular π–π interactions present in structure-optimized DG-Cl, which facilitates the formation of a dense electron cloud. When DG-Cl anchors $TFSI^-$, there is an accumulation of charge on $TFSI^-$ that promotes cleavage of the C–F bond.

To elucidate the formation mechanism of LiF–LiCl, *ab initio* molecular dynamics (AIMD) simulations were employed to analyze the decomposition kinetics of LiTFSI within the PEO-

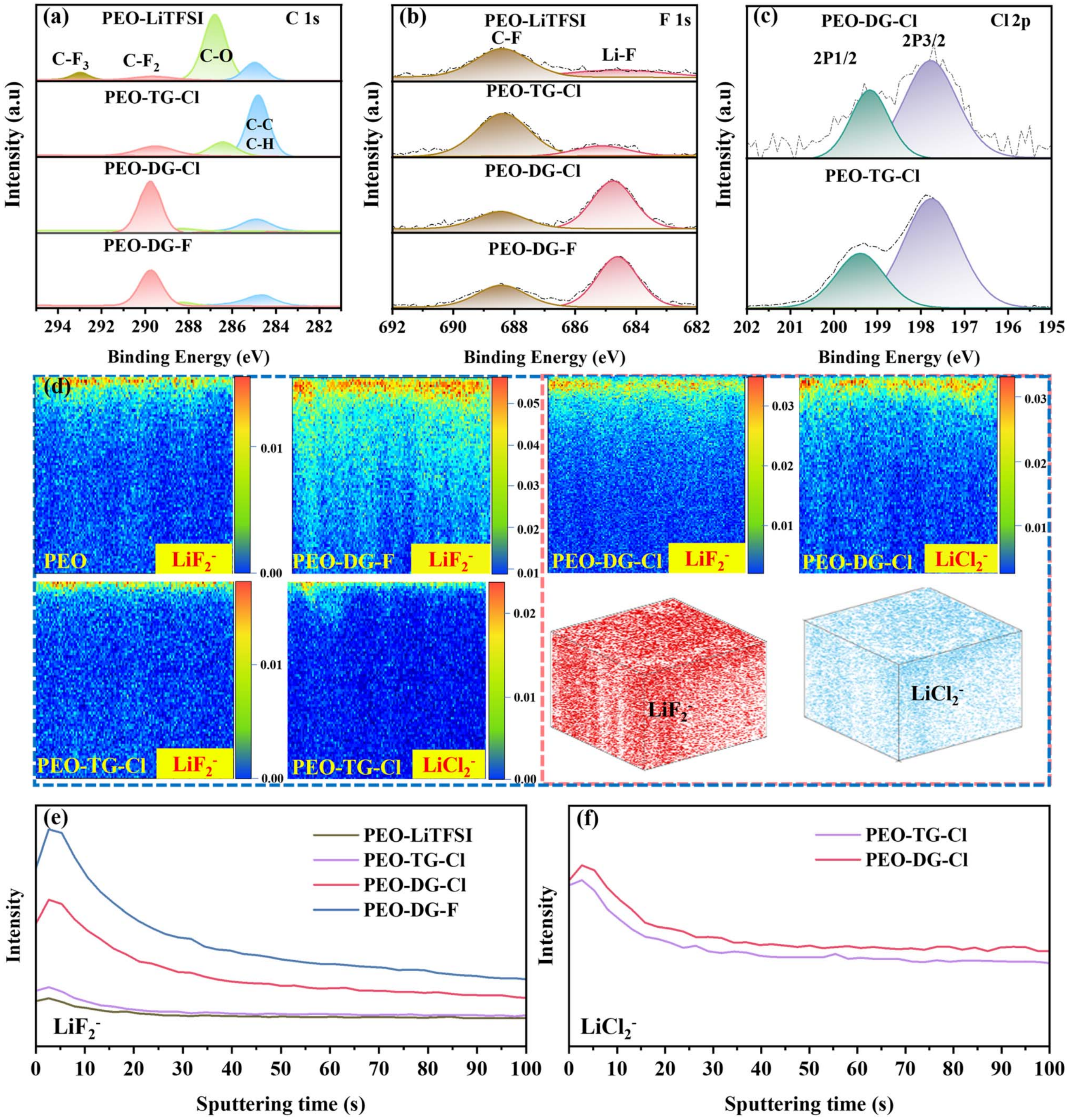

Fig. 4 CSE XPS spectra after 200 h lithium-symmetric cycling: (a) C 1s, (b) F 1s, and (c) Cl 2p. (d) Post-cycling TOF-SIMS characterization of lithium electrodes from CSE batteries. LiF_2^- content mapping and LiF_2^- signals denote LiF. $LiCl_2^-$ content mapping and $LiCl_2^-$ signals denote LiCl. TOF-SIMS 3D reconstruction of PEO-DG-Cl. TOF-SIMS depth profile intensity distribution (e) LiF_2^- and (f) $LiCl_2^-$.

DG-Cl electrolyte system (Fig. 5h). Experimental findings reveal that at 280 fs, a localized transfer of $0.4076e^-$ occurs in the LiTFSI molecule, triggering sequential cleavage of C–S/N–S bonds and simultaneously generating CF_3^-, SO_2^-, and $LiNSO_2CF_2^-$ intermediates. Concurrently, Cl^- in DG-Cl dissociate from their coordination centers and coordinate with Li^+ to form LiCl. By the time point of 520 fs, a directional transfer of $1.1262e^-$ is observed towards $LiNSO_2CF_2^-$, which subsequently dissociates into CF_2^- and $LiNSO_2^-$. At the critical juncture of 760 fs, the C–F bond rupture in the CF_3^- group generates CF_2^- alongside F^-. The F^- then combines with Li^+ to ultimately yield LiF. In conclusion, the results of DFT and AIMD calculations indicate that this functional filler with electronic delocalization can effectively promote the kinetics of F/Cl bond breaking and

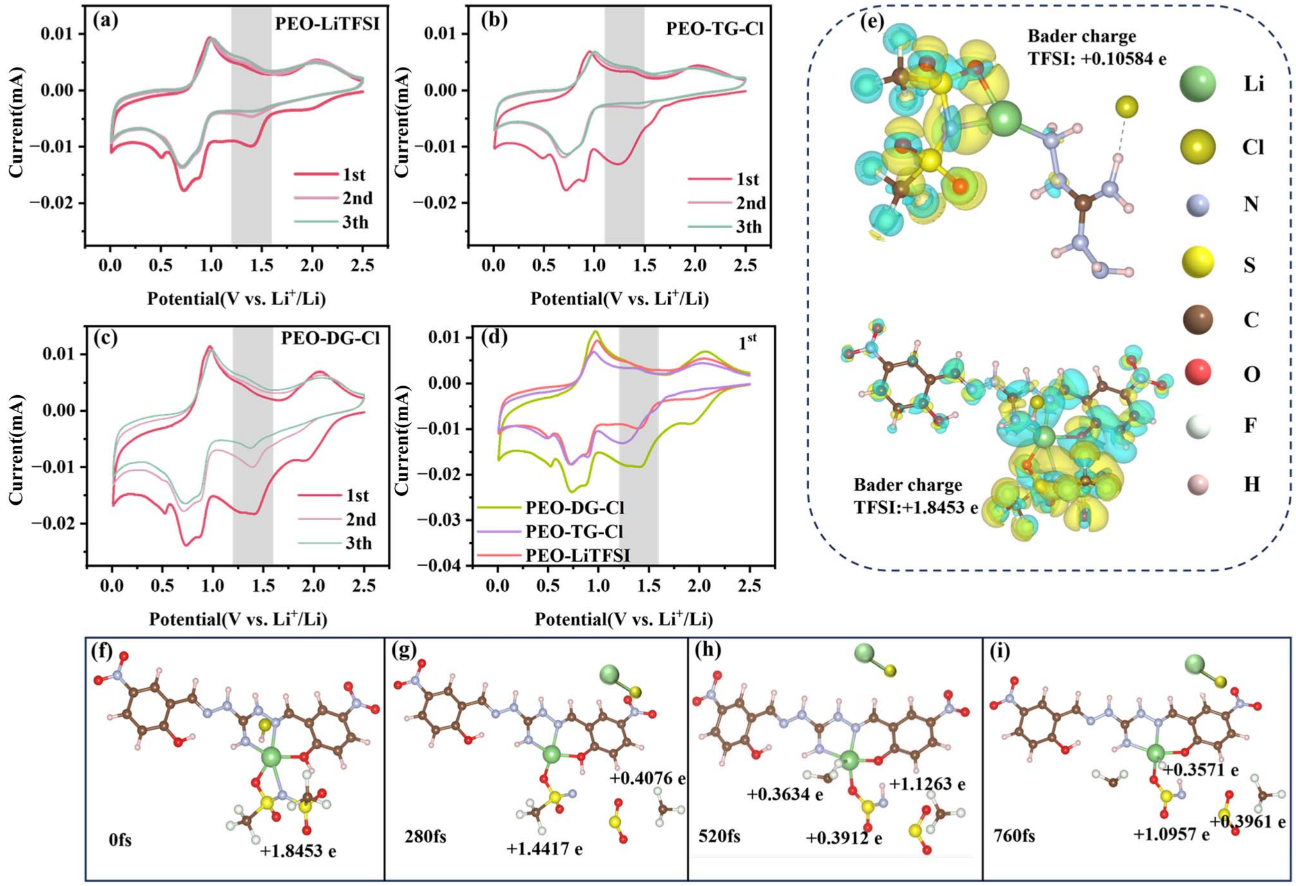

Fig. 5 Li/CSEs/SS CV cycle curves: (a) PEO-LiTFSI, (b) PEO-TG-CL, and (c) PEO-DG-Cl. (d) Initial cyclic voltammetry profiles for four Li/CSEs/SS configurations. (e) Difference in charge density for TG-Cl and DG-Cl. Snapshots of AIMD simulations for PEO-DG-Cl: (f) 0 fs, (g) 280 fs, (h) 520 fs, and (i) 760 fs.

in situ generate a LiF–LiCl-rich SEI, thereby significantly enhancing the electrochemical performance of the battery.

2.5 The electrochemical cycling stability of all-solid-state lithium metal batteries

To investigate the feasibility of LiF–LiCl interfacial modifications for improving cycling durability in solid polymer lithium metal batteries, Li–$LiFePO_4$ (LFP) cells were assembled and tests were conducted at 60 °C. Firstly, long-cycle tests were performed at this temperature. Fig. 6c demonstrates the performance of LFP/PEO-DG-Cl/Li cells at 1C current density. The initial capacity of the battery is measured at 130.6 mAh g^{-1}. After 800 charge–discharge cycles, the reversible capacity decreases to 106.9 mAh g^{-1}, resulting in a capacity retention rate of 82.04%. In addition, the PEO-DG-Cl battery exhibits a relatively small electrode polarization phenomenon (Fig. S6). As depicted in Fig. 6a, for the LFP/PEO-DG-Cl/Li cell operating at a current density of 2C, the initial capacity is recorded as 123.7 mAh g^{-1}. Following 800 cycles, the battery stabilizes at 99.8 mAh g^{-1} with a corresponding capacity retention rate of 80.6%. After 800 cycles, the polarization voltage of the PEO-DG-Cl battery exhibited a relatively stable performance, suggesting that the battery possesses high cycle reversibility (Fig. 6b). Notably, the LFP/PEO-DG-F/Li cell shows markedly inferior performance, commencing with 120.9 mAh g^{-1} initial capacity but deteriorating to 70.6 mAh g^{-1} after equivalent cycling, achieving merely 58.3% retention. Throughout 2C cycling processes, it is observed that both LFP/PEO-LiTFSI/Li and LFP/PEO-TG-Cl/Li cells exhibit lower discharge specific capacities compared to those seen in the LFP/PEO-DG-Cl/Li cell, which ultimately fail after approximately 250 cycles due to performance degradation. Furthermore, it is noteworthy that the discharge specific capacity for the LFP/PEO-TG-Cl/Li cell remains inferior when compared to that achieved by the LFP/PEO-LiTFSI/Li cell. Moreover, the LFP/PEO-TG-Cl/Li battery failed after more than 100 cycles due to severe side reactions.

Subsequently, the rate performance was investigated using galvanostatic testing across multiple current densities (0.1C to 2C), as illustrated in Fig. 6d. Both PEO-DG-Cl and PEO-DG-F electrolytes exhibit enhanced rate performance compared to conventional PEO electrolytes. For the PEO-DG-Cl electrolyte, specific discharge capacities of 159.19, 154.69, 146.16, 136.01, and 120.44 mAh g^{-1} were recorded at 0.1C, 0.2C, 0.5C, 1C, and 2C, respectively, maintaining 154.54 mAh g^{-1} capacity recovery when cycled back to 0.1C. Similarly, the PEO-DG-F electrolytes demonstrated comparable performance with discharge

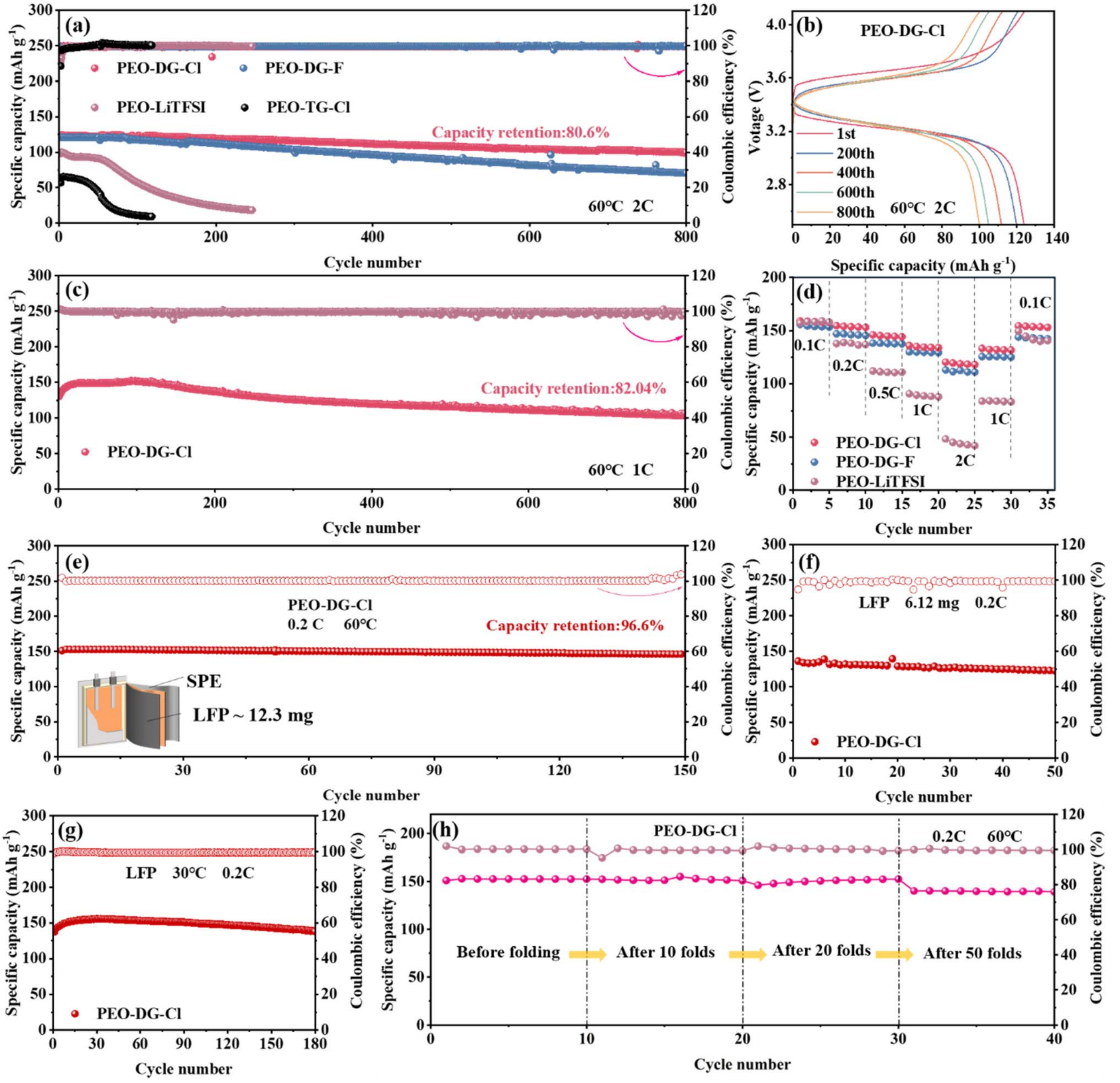

Fig. 6 (a) Cycling performance of LFP/CSEs/Li batteries at 2C. (b) Voltage-specific capacity curve of LFP/PEO-DG-Cl/Li batteries at 2C. (c) Cycling performance of LFP/PEO-DG-Cl/Li batteries operating at 1C. (d) An examination of the cycling performance of LFP/CSEs/Li batteries subjected to various current multiplicities. (e) Cycling performance of the LFP/PEO-DG-Cl/Li pouch cell at 0.2C 60 °C. (f) Cycling performance of an LFP/PEO-DG-Cl/Li battery under high load conditions (LFP: 6.12 mg). (g) Cycling performance of the LFP/PEO-DG-Cl/Li battery at 0.2C 30 °C. (h) Cycling performance of the LFP/PEO-DG-Cl/Li pouch cell at 0.2C and 60 °C before folding, after 10 folds, after 20 folds, and after 50 folds.

capacities of 154.54, 146.30, 138.21, 128.83, and 112.77 mAh g^{-1} under the same testing conditions, retaining 144.8 mAh g^{-1} upon reverting to 0.1C after high rate cycling. Fig. S7 presents voltage curves for LFP/PEO-DG-Cl/Li and LFP/PEO-DG-F/Li batteries under varying charge/discharge conditions. LFP/PEO-DG-Cl/Li consistently exhibits low polarization along with stable charge/discharge platforms. In contrast, the PEO-DG-F electrolyte encounters dendrite penetration leading to short circuits when subjected to elevated currents (specifically observed during testing at 2C). This observation underscores that the PEO-DG-Cl electrolyte possesses exceptional cycling performance under varied current conditions, demonstrating that the LiF–LiCl-rich SEI layer effectively mitigates metallic dendrite propagation, thereby ensuring enhanced cycling stability across diverse operating conditions.

As shown in Fig. 6f, when the active mass loading increased to 6.18 mg, the LFP/PEO-DG-Cl/Li configuration demonstrated an initial specific capacity of 136.2 mAh g^{-1} at a 0.2C rate, which gradually decreased to 122.7 mAh g^{-1} after 50 cycles. Due to the low ionic conductivity of traditional PEO electrolytes at room temperature, their cycling performance at room temperature is poor. However, the introduction of the filler DG-Cl enhances the ionic conductivity. Therefore, we evaluated the cycling performance of LFP/PEO-DG-Cl/Li at room temperature. As shown in Fig. 6g and S8, the PEO-DG-Cl battery exhibited enhanced performance characteristics at a current density of 0.2C, maintaining 130.2 mAh g^{-1} initial discharge capacity through 180 cycles without notable degradation, demonstrating improved low-temperature functionality. Furthermore, in order to explore the potential compatibility of PEO-DG-Cl with high-voltage cathodes, an NCM811/PEO-DG-Cl/Li battery was assembled using $LiNi_{0.8}Co_{0.1}Mn_{0.1}O_2$ (NCM811) as the cathode material. This battery demonstrated 156.1 mAh g^{-1} initial capacity at 0.2C, retaining 71.2% capacity after seventy cycles (Fig. S9). To evaluate the practical applicability of the LFP/PEO-DG-Cl/Li battery, a soft-pack battery was assembled for cycling tests (Fig. 6e). The initial discharge specific capacity of the pouch cell at a rate of 2C was measured at 151 mAh g^{-1}. After undergoing 150 cycles, the discharge specific capacity decreased to 145.9 mAh g^{-1}, resulting in a capacity retention rate of 96.6%. To verify the flexible applicability of the pouch cell, a small bulb was used to conduct illumination tests under bending, puncture, and cutting conditions (Fig. S10). Additionally, the cycling performance of the pouch cell was evaluated after 10, 20, and 50 folds, as depicted in Fig. 6h. The capacity remained largely unchanged after 10 and 20 folds, while a pronounced decline was observed following 50 folds. Experimental results demonstrated that, although a certain degree of capacity degradation occurred during the testing process, the battery was able to maintain a stable and safe operational state throughout the entire duration, with the bulb remaining continuously illuminated.

3 Conclusion

In this work, a π-conjugated organic ionic salt (DG-Cl) with enhanced electron delocalization capability was prepared to catalyze the *in situ* formation of a stable SEI. Specifically, the Cl^- ions of DG-Cl dissociate under the electric field and subsequently combine with Li^+ to form LiCl. Then, DG^+ with abundant cation vacancies restricts the movement of $TFSI^-$ and promotes efficient charge transfer to $TFSI^-$ by leveraging its π-conjugated electron delocalization effect, which results in the generation of additional LiF. Notably, the DFT results reveal that the structurally modified DG-Cl exhibits a charge transfer number of $1.8453e^-$, which is 17 times higher than that of the unmodified TG-Cl ($0.10584e^-$). This demonstrates the powerful charge delocalization function of DG-Cl, thereby promoting the co-growth of LiF–LiCl-rich SEIs. Experimental results demonstrate that the battery performance based on the LiF–LiCl-rich SEI surpasses that of a single SEI dominated by LiF alone. Owing to the enhanced ability of the LiF–LiCl rich SEI to inhibit lithium dendrite formation and mitigate side reactions, Li/PEO-DG-Cl symmetric cells demonstrate excellent cycling performance over 4000 hours at 0.1 mA cm^{-2}, significantly better than that of PEO-DG-F (2000 hours). Furthermore, the Li/PEO-DG-Cl/LFP full cell delivers a capacity retention of 80.6% after 800 cycles at a rate of 2C. This strategy of enhancing electronic delocalization at the molecular structure level has verified its feasibility and potential value in practical applications in the field of energy storage.

Author contributions

S. Su performed the chemical research and prepared the manuscript; X. Zhou helped with XPS, SEM, and TOF-SIMS characterization; W. Liang contributed to the DFT calculation; Z. Su helped with pouch cell assembly and performance testing; Y. Qu helped with electrochemical testing; Y. Zh helped with the physical tests of the electrolyte; J. Qiu helped collate and organize the data; B. Zhang conceived the idea and designed the research. All authors have given approval to the final version of the manuscript.

Conflicts of interest

The authors declare that they have no known competing financial interests or personal relationships that could have appeared to influence the work reported in this paper.

Data availability

The data that support the findings of this study are available from the corresponding author upon reasonable request. Source data are provided in this paper.

The data supporting this article have been included as part of the SI. Supplementary information: sample preparation, testing methods, and partial sample characterization. See DOI: https://doi.org/10.1039/d5sc05254h.

Acknowledgements

The authors acknowledge support from the China Postdoctoral Science Foundation (2024M763135), the Outstanding Youth Project of Education Bureau of Hunan Province (23B0161), the Natural Science Foundation of Hunan Province(2024JJ5376), the College Students Innovation and Entrepreneurship Training Program of Hunan Province (S202410530061), the Chenzhou National Sustainable Development Agenda Innovation Demonstration Zone Construction Project (CN) (2023sfq65), and the Undergraduate Innovation and Entrepreneurship Training Program of Hunan Province (No. S202510530260 and S202510530177).

References

1 D. Li, H. Liu, C. Wang, C. Yan, Q. Zhang, C. W. Nan and L. Z. Fan, High ionic conductive, mechanical robust sulfide solid electrolyte films and interface design for all-solid-state lithium metal batteries, *Adv. Funct. Mater.*, 2024, **34**, 2315555.

2 Y. Zhang, S. Jing, H. Shen, S. Li, Y. Huang, Y. Shen, S. Liu, Z. Zhang and F. Liu, Developments, Novel Concepts, and Challenges of Current Collectors: From Conventional

Lithium Batteries to All-Solid-State Batteries, *ChemElectroChem*, 2024, **11**, e202300739.

3 Y. Ren, S. Chen, M. Odziomek, J. Guo, P. Xu, H. Xie, Z. Tian, M. Antonietti and T. Liu, Mixing Functionality in Polymer Electrolytes: A New Horizon for Achieving High-Performance All-Solid-State Lithium Metal Batteries, *Angew. Chem., Int. Ed.*, 2025, **64**, e202422169.

4 D. Hu, H. Huang, C. Wang, Q. Hong, H. Wang, S. Tang, H. Zhang, J. Li, L. Hu and L. Jiang, Tailoring Multiple Interactions in Poly (Urethane-Urea)-Based Solid-State Polymer Electrolytes for Long-Term Cycling Lithium Metal Batteries, *Adv. Energy Mater.*, 2024, **15**, 2406176.

5 H. Du, Y. Wang, Y. Kang, Y. Zhao, Y. Tian, X. Wang, Y. Tan, Z. Liang, J. Wozny and T. Li, Side reactions/changes in lithium-ion batteries: mechanisms and strategies for creating safer and better batteries, *Adv. Energy Mater.*, 2024, **36**, 2401482.

6 H. Wang, D. Yan, H. Liu, S. Li, X. Niu, C. Ouyang, H. Li and L. Wang, A Non-Concentrated Gradient-Solvation Electrolyte Enables a High-Voltage Lithium Metal Battery with 447.6 Wh Kg^{-1}, *Adv. Mater.*, 2025, 2509760.

7 X. Yue, C. Ma, J. Bao, S. Yang, D. Chen, X. Wu and Y. Zhou, Failure mechanisms of lithium metal anode and their advanced characterization technologies, *Acta Phys.-Chim. Sin.*, 2021, **37**, 2005012.

8 Q. Xu, T. Li, Z. Ju, G. Chen, D. Ye, G. I. Waterhouse, Y. Lu, X. Lai, G. Zhou and L. Guo, $Li_2ZrF_6^-$ based electrolytes for durable lithium metal batteries, *Nature*, 2025, **637**, 339–346.

9 Q. Liu, J. Yu, W. Guo, Y. Pan, C. Han, H. b. Liu and B. Li, Boosting the Li| LAGP interfacial compatibility with trace nonflammable all-fluorinated electrolyte: The role of solid electrolyte interphase, *Ecomat*, 2023, **5**, e12322.

10 H. Wan, B. Zhang, S. Liu, Z. Wang, J. Xu and C. Wang, Interface Design for High-Performance All-Solid-State Lithium Batteries, *Adv. Energy Mater.*, 2024, **14**, 2303046.

11 D. Yan, Y. Ma, H. Wang, W. Jia, X. Niu, H. Wang, W. Zou and L. Wang, High ionic conductivity conjugated artificial solid electrolyte interphase enabling stable lithium metal batteries, *Green Chem.*, 2025, **27**, 7564–7574.

12 C. Jin, A. Xiang, Z. Wang, Q. He, B. Li, X. Zhang, Y. Xiang, P. Zhai and Y. Gong, Anion-Reduction-Catalysis Induced LiF-Rich SEI Construction for High-Performance Lithium-Metal Batteries, *Adv. Energy Mater.*, 2025, **15**, 2402811.

13 S. Yan, H. Liu, Y. Lu, Q. Feng, H. Zhou, Y. Wu, W. Hou, Y. Xia, H. Zhou and P. Zhou, Selectively fluorinated aromatic lithium salts regulate the solvation structure and interfacial chemistry for all-solid-state batteries, *Sci. Adv.*, 2025, **11**, eads4014.

14 K. Li, Z. Wang, B. Yang, T. Li, B. Li, J. Chen, Z. Yan, M. He, A. Hu and J. Long, Elucidating the role of polar functional groups in fluorinated polymer artificial interphase for stable lithium anodes, *Chem. Eng. J.*, 2024, **493**, 152527.

15 Z. Chen, J. Pan, W. Huang, K. Shi, Z. Yang, H. Wu, S. Wei, G. Jiang, W. Zou and R. Zhang, Heterogeneity-Segment Charge-Induced-Coupling Catalysis of Component-Selective-Type Covalent Organic Frameworks Interface toward Stabilizing Lithium Metal Anode, *ACS Nano*, 2025, **19**, 13160–13174.

16 F. Chu, J. Zhou, J. Liu, F. Tang, L. Song and F. Wu, Constructing a fluorinated interface layer enriched with Ge nanoparticles and Li-Ge alloy for stable lithium metal anodes, *Nano Res.*, 2024, **17**, 5148–5158.

17 Y. Wang, Z. Wu, F. M. Azad, Y. Zhu, L. Wang, C. J. Hawker, A. K. Whittaker, M. Forsyth and C. Zhang, Fluorination in advanced battery design, *Nat. Rev. Mater.*, 2024, **9**, 119–133.

18 J. Wang, L. Chen, H. Li and F. Wu, Anode interfacial issues in solid-state Li batteries: mechanistic understanding and mitigating strategies, *Energy Environ. Mater.*, 2023, **6**, e12613.

19 H. Duan, C. Wang, S. Zhang, J. Fu, W. Li, J. Wan, R. Yu, M. Fan, F. Ren and S. Wang, Amorphous AlOCl Compounds Enabling Nanocrystalline LiCl with Abnormally High Ionic Conductivity, *J. Am. Chem. Soc.*, 2024, **146**, 29335–29343.

20 P. Ren, N. S. Grundish, S. Zhang, L. Zhou, R. Liu, N. Wu and Y. Li, Scalable Interfacial Engineering with Lithiophilic-Lithiophobic Layers for High-Performance All-Solid-State Li-Metal Batteries, *Adv. Funct. Mater.*, 2025, 2501573.

21 K. Zhang, F. Wu, K. Zhang, S. Weng, X. Wang, M. Gao, Y. Sun, D. Cao, Y. Bai and H. Xu, Chlorinated dual-protective layers as interfacial stabilizer for dendrite-free lithium metal anode, *Energy Storage Mater.*, 2021, **41**, 485–494.

22 M. B. Mogensen and E. Hennesø, Properties and Structure of the LiCl-Films on Lithium Anodes in Liquid Cathodes, *Acta Chim. Slov.*, 2016, **63**, 519–534.

23 J. Cao, G. Du, G. Qian, X. Lu, Y. Sun and X. Lu, Li Alloy/Li Halide Mixed Layer: An Emerging Star for Electro-Chemo-Mechanically Stable Li/Electrolyte Interface, *Electrochem. Energy Rev.*, 2024, **7**, 31.

24 D. Ding, H. Ma, H. Tao, X. Yang and L. Fan, Stabilizing a $Li_{1.3}Al_{0.3}Ti_{1.7}(PO_4)_3$/Li metal anode interface in solid-state batteries with a LiF/Cu-rich multifunctional interlayer, *Chem. Sci.*, 2024, **15**, 3730–3740.

25 Y. Yang, S. Biswas, R. Xu, X. Xiao, X. Xu, P. Zhang, H. Gong, X. Zheng, Y. Peng and J. Li, Capacity recovery by transient voltage pulse in silicon-anode batteries, *Science*, 2024, **386**, 322–327.

26 B. Wang, P.-Z. Zhang, X. Chen and A. Q. Jia, Syntheses and crystal structures of guanidine hydrochlorides with two Schiff base functions as efficient colorimetric and selective sensors for fluoride. Jia, *Z. Naturforsch., B*, 2018, **73**, 601–609.

27 X. Liu, Y. Jin, H. Wang, X. Yang, P. Zhang, K. Wang and J. Jiang, In situ growth of covalent organic framework nanosheets on graphene as the cathode for long-life high-capacity lithium-ion batteries, *Adv. Mater.*, 2022, **34**, 2203605.

28 T. Prakasam, S. K. Sharma, F. Ravaux, F. Benyettou, M. Lusi, V. Sabu, P. Bazin, T. Delclos, R. Jagannathan and J. Whelan, 2D covalent organic framework *via* catenation, *Chem*, 2025, **11**, 102307.

29 H. De Groot, G. Harbison, J. Herzfeld and R. Griffin, Nuclear magnetic resonance study of the Schiff base in

bacteriorhodopsin: counterion effects on the nitrogen-15 shift anisotropy, *Biochemistry*, 1989, **28**, 3346–3353.

30 E. D. Becker, *High resolution NMR: theory and chemical applications*, Elsevier, 1999.

31 R. M. Silverstein and G. C. Bassler, Spectrometric identification of organic compounds, *J. Chem. Educ.*, 1962, **39**, 546.

32 H. Liang, L. Wang, A. Wang, Y. Song, Y. Wu, Y. Yang and X. He, Tailoring practically accessible polymer/inorganic composite electrolytes for all-solid-state lithium metal batteries: a review, *Nano-Micro Lett.*, 2023, **15**, 42.

33 P. Selig, Guanidine Organocatalysis, *Synthesis*, 2013, **45**, 703–718.

34 S. Yang, A. Chen, Z. Tang, Z. Wu, P. Li, Y. Wang, X. Wang, X. Jin, S. Bai and C. Zhi, Regulating the Electrochemical Reduction Kinetics by the Steric Hindrance Effect for a Robust Zn Metal Anode, *Energy Environ. Sci.*, 2024, **17**, 1095–1106.

35 W. Liu, X.-M. Wang, D. Li, Y. Gao, K. Wang and X. Huang, Dominant Mechanism of Nanofiltration for Chloride/Sulfate Ion Separation in High Salinity Solutions: The Quantification of Pore Size-Influenced Dielectric Exclusion, *Environ. Sci. Technol.*, 2025, **59**, 5848–5855.

36 J. Zhou, C. Chen, J. Sun, T. R. Fielitz, W. Zhou, D. G. Cahill and P. V. Braun, Reduction of the Thermal Conductivity of Polyurethanes by Fluorination: Impact of Crystallinity, Atomic Density, and Sound Velocity, *Angew. Chem.*, 2025, e202503497.

37 X. Chen, R. Zhan, Z. Chen, X. Wang, S. Tu, S. Liu, Y. Zeng, T. Dong and K. Cheng, Enhancing Fast-Charging Capability of Thick Electrode in Lithium-Ion Batteries Through Electronic/Ionic Hybrid Conductive Additive Engineering, *Adv. Energy Mater.*, 2025, **64**, 2500242.

38 X. Wang, B. He, B. Liu, M. Avdeev and S. Shi, A Database of Electrochemical Stability Windows Containing over 1500 Solid-State Inorganic Compounds, *Adv. Funct. Mater.*, 2024, **34**, 2406146.

39 W. Liu, J. Liu, Z. Yang, M. Liu, S. Sang and H. Liu, Flaky Li-Doped High-Entropy Oxide Enables PEO-Based Composite Solid Electrolyte with Extended Suitability for Lithium Metal Batteries, *Adv. Funct. Mater.*, 2024, **35**, 2419095.

40 Z. Zhao, X. Zhou, B. Zhang, F. Huang, Y. Wang, Z. Ma and J. Liu, Regulating Steric Hindrance of Porous Organic Polymers in Composite Solid-State Electrolytes to Induce the Formation of LiF-Rich SEI in Li-Ion Batteries, *Angew. Chem., Int. Ed.*, 2023, **62**, e202308738.

41 Q. Ye, H. Liang, S. Wang, C. Cui, C. Zeng, T. Zhai and H. Li, Fabricating a PVDF skin for PEO-based SPE to stabilize the interface both at cathode and anode for Li-ion batteries, *J. Energy Chem.*, 2022, **70**, 356–362.

42 Y. Guo, M. Zhang, Z. Ge, Z. Fang, Z. Xu, J. Wu and M. Wu, Electrostatic Force-Tailored PEO-Based Solid Electrolyte with Fast Li^+ Transport for Ultra-Robust Lithium Metal Batteries, *Adv. Funct. Mater.*, 2025, **35**, 2419998.

43 Y. Yi, R. Yu, W. Li, Y. Jin and Z. Dai, Preparation of Mo, Al-doped $Li_7La_3Zr_2O_{12}$-based composite solid electrolyte and performance of all-solid-state batterys, *Energy Storage Sci. Technol.*, 2023, **12**, 1490.

44 J. Shen, S. Liu, X. Han, Z. Chen, W. Tian, C. Yang, H. Pan, S. Chen and S. Zhu, Regulating the Li–O coordination in polymer electrolytes *via* semi-ionic CF bonds for high-voltage solid lithium metal batteries, *Chem. Eng. J.*, 2024, **484**, 149497.

45 C. He, H. Ying, L. Cai, H. Chen, Z. Xu, S. Liu, P. Huang, H. Zhang, W. Song and J. Zhang, Tailoring Stable PEO-Based Electrolyte/Electrodes Interfaces *via* Molecular Coordination Regulating Enables 4.5 V Solid-State Lithium Metal Batteries, *Adv. Funct. Mater.*, 2024, **34**, 2410350.

46 J. Yang, R. Li, P. Zhang, J. Zhang, J. Meng, L. Li, Z. Li and X. Pu, Crosslinked polymer-in-salt solid electrolyte with multiple ion transport paths for solid-state lithium metal batteries, *Energy Storage Mater.*, 2024, **64**, 103088.

47 Y. Xia, Q. Wang, Y. Liu, J. Zhang, X. Xia, H. Huang, Y. Gan, X. He, Z. Xiao and W. Zhang, Three-dimensional polyimide nanofiber framework reinforced polymer electrolyte for all-solid-state lithium metal battery, *J. Colloid Interface Sci.*, 2023, **638**, 908–917.

48 J. Cheng, X. Ci, H. Zhang, Z. Zeng, X. Zhou, Y. Li, H. Qiu, W. Zhai, D. Gao and L. Ci, Unlocking oxygen vacancy-rich high-entropy oxides in upgrading composite solid electrolyte, *Rare Met.*, 2024, **44**, 961–972.

49 J. Zhao, M. Xie, H. Zhang, R. Yi, C. Hu, T. Kang, L. Zheng, R. Cui, H. Chen and Y. Shen, In situ modification strategy for development of room-temperature solid-state lithium batteries with high rate capability, *Acta Phys.-Chim. Sin.*, 2021, **37**, 2104003.

50 C. Wang, T. Wang, L. Wang, Z. Hu, Z. Cui, J. Li, S. Dong, X. Zhou and G. Cui, Differentiated lithium salt design for multilayered PEO electrolyte enables a high-voltage solid-state lithium metal battery, *Adv. Sci.*, 2019, **6**, 1901036.

51 M. Iqbal, M. Muneer, R. Raza, M. Saleem, S. Hussain, Z. U. Rehman, F. Abbas, S. Ali, M. A. Javed and M. Hussain, Recycling of lead from lead acid battery to form composite material as an anode for low temperature solid oxide fuel cell, *Mater. Today Energy*, 2020, **16**, 100418.

52 F. Tao, K. Yan, C. Dong, J. Wang, Q. Pan, M. Gong, J. Gu, C. Shen, R. Yu and Y. Jiang, Electric-Dipole Coupling Ion-Dipole Engineering Induced Rational Solvation-Desolvation Behavior for Constructing Stable Solid-State Lithium Metal Batteries, *Angew. Chem.*, 2025, **137**, e202503037.

53 S. Zhang, Y. Li, L. J. Bannenberg, M. Liu, S. Ganapathy and M. Wagemaker, The lasting impact of formation cycling on the Li-ion kinetics between SEI and the Li-metal anode and its correlation with efficiency, *Sci. Adv.*, 2024, **10**, eadj8889.

54 T. Li, Q. Zheng, J. Li, Z. Zhao, W. Huang, B. Zhang, G. Zhao, T. Wu, D. Peng and Q. Xie, Molecular-level Regulation of PEO-Based Electrolytes with CaF_2 Nanoparticles for Advanced Solid-State Lithium Metal Batteries, *ACS Energy Lett.*, 2025, **10**, 2228–2235.

55 D. Hu, H. Huang, C. Wang, Q. Hong, H. Wang, S. Tang, H. Zhang, J. Li, L. Hu and L. Jiang, Tailoring Multiple Interactions in Poly (Urethane-Urea)-Based Solid-State

Polymer Electrolytes for Long-Term Cycling Lithium Metal Batteries, *Adv. Energy Mater.*, 2025, **15**, 2406176.

56 Z. Zhao, L. Kong, J. Sun, Y. Li and W. Feng, Fluorinated polymer-derived microporous carbon spheres for CFx cathodes with high energy density, *Giant*, 2024, **18**, 100273.

57 L. Xu, S. Li, H. Tu, F. Zhu, H. Liu, W. Deng, J. Hu, G. Zou, H. Hou and X. Ji, Molecular engineering of highly fluorinated carbon dots: tailoring Li^+ dynamics and interfacial fluorination for stable solid lithium batteries, *ACS Nano*, 2023, **17**, 22082–22094.

58 A. Sun, H. Tu, Z. Sun, Z. He, Y. Wang, J. Wang, Y. Zheng, F. Zhu, L. Wang and F. Mushtaq, Dual-Halide Interphase Enabling High-Performance Lithium Metal Batteries in Wide-Temperature Range, *ACS Energy Lett.*, 2024, **9**, 2545–2553.

59 Y. Xu, H. Jia, P. Gao, D. E. Galvez-Aranda, S. P. Beltran, X. Cao, P. M. Le, J. Liu, M. H. Engelhard and S. Li, Direct *in situ* measurements of electrical properties of solid-electrolyte interphase on lithium metal anodes, *Nat. Energy*, 2023, **8**, 1345–1354.